Economic Optimization of an Integrated Regenerative Transcritical Cycle with a Small Modular Reactor

Jacob Bryan[1,*], Yili Zhang[1], Hailei Wang[1], Geordie Richards[1]

Abstract

Small modular reactors (SMRs) are a promising new technology due to their potential benefits to cost, ease of manufacturing, and safety. One such SMR is the NuScale Power Module (NPM), a pressurized light water reactor driven by natural convection. Previous works have shown that organic regenerative transcritical cycles (ORTCs) with methanol as a working fluid can have superior performance in medium-temperature applications compared to other cycle designs and working fluids. In this study, a techno-economic optimization is performed on the combined NPM primary cycle and an ORTC secondary cycle. This optimization problem is subject to nonlinear, hidden (not explicit) constraints, which significantly increases the computational complexity of the problem. The parametric design points resulting from several optimization algorithms and objective functions are compared. Design points which minimize LCOE tend to seek to minimize the need for regenerators in the ORTC, with these LCOE-optimal designs reducing the LCOE by approximately 19%. This optimal design lies very close to one of the hidden constraint boundaries; a locally-valid explicit formulation for this constraint is presented. The secondary cycle design points presented here may significantly reduce the LCOE of SMRs and warrant further analysis and experimental validation.

Keywords: economic optimization, small modular reactor, transcritical cycle, organic Rankine cycle

Nomenclature

Symbols

$\dot{m}$	Mass flow rate
$\dot{W}$	Power
η_a	Wet-steam turbine efficiency
η_I	First law efficiency
P_{max}	Maximum pressure of the secondary cycle
x_a	Baumann quality
x_{in}	Pump inlet vapor quality
$x_{isen,out}$	Isentropic outlet vapor quality
a	Baumann factor
f	Splitter mass fraction
h	Enthalpy

---

*Corresponding Author

Email addresses: `jacob.bryan@usu.edu` (Jacob Bryan), `yili.zhang@usu.edu` (Yili Zhang), `hailei.wang@usu.edu` (Hailei Wang), `geordie.richards@usu.edu` (Geordie Richards)

P	Pressure
R	Turbine pressure ratio
s	Entropy
T	Temperature
x	Lengthwise/axial direction

Subscripts

C	Cold side
des	Desired state value
f	Saturated liquid
g	Saturated vapor
H	Hot side
in	Inlet value
isen	Isentropic
max	Maximum value
min	Minimum value
out	Outlet value
P	Primary side
p	Pump
pinch	Value at the pinch point (at minimum temperature difference)
pump	Pump inlet value
S	Secondary side
sat	Value at saturation
t	Turbine
tot	Total value
turb	To turbine
u	Upstream value; particularly, the fluid entering a mixing valve from the cold side exit of a previous regenerator

1. Introduction

World energy demand was approximately 14,314 Mtoe in 2018, 81% of which came from fossil fuel sources, and is expected to grow by up to 33.6% by 2040 [1]. Despite falling prices of many renewable energy sources, such as wind and photovoltaic solar, there remains the problem of finding carbon-free alternatives to replace existing non-renewable sources and meet growing base-load demands; nuclear energy is a promising solution, particularly due to having the highest capacity factor of any energy source [2].

However, nuclear energy has long been plagued by high costs relative to other energy sources [3]. In particular, large nuclear plants suffer from high capital construction costs and expensive operational costs. Small modular reactors (SMRs) are a promising technology that may help to reduce these costs by utilizing faster, factory-based construction methods and taking advantage of economies of scale [4].

One such SMR is the NuScale Power Module (NPM), designed by NuScale Power. The NPM is cooled by natural convection with pressurized water, operating at 12.8 MPa and a maximum temperature of 310°C. Each module is currently designed to produce 160 MW_t; up to 12 modules can be monitored and operated at a single plant. NuScale originally estimated the LCOE for a 12-unit plant to be \$86/MWh (as of 2016), but With recent updates to designed power output, they hope to be able to provide energy at \$65/MWh [5, 6]. A cost-effective secondary power cycle could help to reach this goal.

The secondary cycle would need to take advantage of the mid-grade heat (typically 500 K - 800 K) generated by the NPM. Organic Rankine cycles (ORCs) are commonly used in low- and mid-grade heat applications [7, 8, 9, 10, 11, 12]. Maraver et al. [13] provides a systematic look at ORC design and optimization criteria for a number of fluids and primary heat exchanger temperature profiles. They found that an ORC benefited from a recuperator if there is a lower limit on the outlet temperature of the heat source, and that trascritical operation can be beneficial if it helps the lower temperature fluid better match the temperature profile of the heat source fluid in the primary heat exchanger.

Two recent works have explored organic transcritical regenerative cycles (ORTCs) for mid-grade heat application. Surendran and Seshadri [14] proposed a novel transcritical renegerative series two stage organic rankine cycle for a dual source, mid-grade heat application. This novel cycle had a net power increase of 15-34% and 15-52% relative to series two stage and single stage ORCs, respectively. Zhang et al. [15] proposed an ORTC to operate in conjunction with the NPM specifically and presented a method for modeling the integrated cycles. Their work proposed using methanol as a working fluid in this secondary cycle, due to its superior performance with the mid-grade temperatures produced by the NPM. This design appears to be a viable alternative to more typical steam Rankine cycles for this application, despite little optimization work having been done in that study.

Many examples of global optimizations of thermodynamic cycles exist in the literature. The majority of these works rely on genetic algorithms (GA), simulated annealing (SA) methods, and particle swarm optimization (PSO) methods. All of these global optimization methods employ some form of stochastic element to avoid getting stuck in a local minimum while searching for the global minimum, which is essential for minimizing a non-convex objective function. Recent examples include Sun et al. [10], Bakhshmand et al. [16], Clarke et al. [17], and [18]. Sun et al. [10] compared two ORC configurations over a range of heat source temperatures. These configurations were defined by up to 7 design parameters, and a PSO algorithm was used to optimize each configuration. Bakhshmand et al. [16] used a GA to perform an exergoeconomic optimization on a combined cycle power plant specified by 13 design variables. Clarke et al. [17] compared the use of GA and PSO algorithms for optimizing a geothermal power plant, finding that the PSO method gave superior results at less computational expense in the case of their 2-variable optimization problem. Wang et al. [18] used a SA method to optimize an ORC for waste heat recovery with 4 parameters.

This current study builds directly upon the work of Zhang et al. [15] by performing a thorough optimization of the ORTC presented there. Literature regarding the performance of ORTCs is sparse, especially for mid-grade heat applications. No other works used methanol as a working fluid. Performing a thorough optimization of the secondary cycle at hand will provide an example of the economic gains possible with such an ORTC.

Section 2 details the mathematical model for the integrated cycles. Section 3 outlines the optimization methods used in this study. The results of the optimization and an analysis of the resulting optima is presented in Section 4. This includes a comparison of design points resulting from optimizing for LCOE and for first law efficiency. Finally, the conclusions of this study are summarized in Section 5.
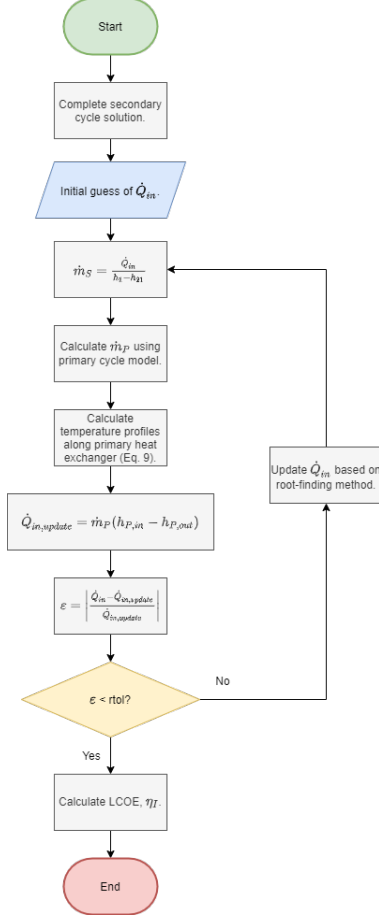
Figure 1: Diagram of the integrated cycles solution method.

Note that this optimization is performed with a cost model developed in 2017 and uses the 2016 NuScale design as a baseline. As such, all LCOE values provided here are in 2016 dollars.

2. Modeling of the Integrated Cycles

The work in Zhang et al. [15] set a foundation for modeling the integrated NPM primary cycle and ORTC secondary cycle. In this section, a number of algorithmic improvements to the solution method are presented which severely reduce the solution time of the model.

This section details the integrated cycles model developed for the integrated NPM primary cycle and the ORTC secondary cycle. The design of the secondary cycle and its component models remain largely unchanged from Zhang et al. [15], with the exception of a new pump/regenerator solution technique. However, several algorithmic changes have been made to the integrated cycles solution method which nearly decouple the primary and secondary cycle solutions. The only remaining dependence is in solving the total heat transfer rate from the primary cycle to the secondary cycle ($\dot{Q}_{in}$) and the impact this has on the designed mass flow rate in the secondary cycle. Additionally,

The solution method for the primary heat exchanger, which couples the primary and secondary cycles, is also unchanged. The system of differential equations used to model this heat exchanger are briefly reviewed here, but readers are referred to Zhang et al. [15] for further details.

The overall solution method for the integrated cycle model is found in Fig. 1. A secant method was used for the root-finding method here due to being a gradient-free method that showed to be both faster and more stable than the fixed point iteration method used previously, given appropriate initial guesses for $\dot{Q}_{in}$.

4

2.1. Secondary Cycle

The design of the secondary cycle is parameterized by seven design variables: the maximum cycle pressure (P_{max}); the pressure ratios of the high-, mid-hi-, and mid-low-pressure turbines (R_1, R_2, and R_3, respectively); and the splitter valve fractions (f_1, f_2, and f_3, respectively). Together, these design variables uniquely define the pressure and fraction of the total mass flow rate everywhere in the cycle. A diagram of the cycle design can be found in Fig. 3.

P_{max} is allowed to vary between 8.22 and 9.2 MPa. The study by Zhang et al. [15] indicated that the cycle performs best when designed close to the critical pressure. The critical pressure of methanol is approximately 8.216 MPa, so a lower bound of the maximum pressure at 8.22 MPa lies close to the critical pressure but is also sufficiently far from it to ensure that REFPROP 10.0, the equation of state-based thermodynamic property solver employed here, would produce reliable results. The maximum value of 9.2 MPa is rather arbitrary and is meant to allow for sufficient design flexibility in the event of unexpected results but still maintain the sampled design points relatively close to the critical pressure. The pressure ratios and splitting valve fractions can vary between 0 and 1.

A number of other essential parameters in the design were held constant. Specifically, the minimum and maximum cycle temperatures are fixed at 35°C and 301°C, respectively, and the pump and turbine efficiencies are held at 75% and 85%, respectively.

The component models used to model the secondary cycle are detailed in their respective subsections below, and a diagram of the solution method is included in Fig. 2.

2.1.1. Turbines

The turbines are modeled with the Baumann model for wet-steam turbines,

$$\dot{W}_t = \eta_a \dot{m}_C (h_{in} - h_{isen,out}) \tag{1}$$

$$\eta_a = \eta_t \left[1 - a(1 - x_a) \right] \tag{2}$$

$$x_a = \frac{x_{in} + x_{isen,out}}{2}, \tag{3}$$

with Baumann factor $a = 0.72$ [19, 20]. The Baumann quality, x_a, is defined as the average of the inlet and isentropic outlet vapor qualities. The turbine efficiency is assumed to be $\eta_t = 0.85$.

2.1.2. Pumps

The pumps operate with an assumed efficiency of $\eta_p = 0.75$ and are modeled according to

$$\dot{W}_p = \frac{\dot{m}(h_{isen,out} - h_{in})}{\eta_p}. \tag{4}$$

The pump outlet enthalpy is then defined by

$$h_{out} = h_{in} + \frac{\dot{W}_p}{\dot{m}}. \tag{5}$$

It is essential for pump operation for the fluid in the pump to be a liquid. For this reason, the fluid entering the pump is desired to be subcooled by at least 1°C, though any solution which had no vapor in the fluid at the pump inlet is accepted. Any design which would require the fluid at the pump inlet to have any vapor is not considered a valid design.

2.1.3. Regenerators

The regenerators are modeled as counterflow heat exchangers. By conservation of energy and assuming negligible heat loss to the environment, the regenerator fluid states satisfy

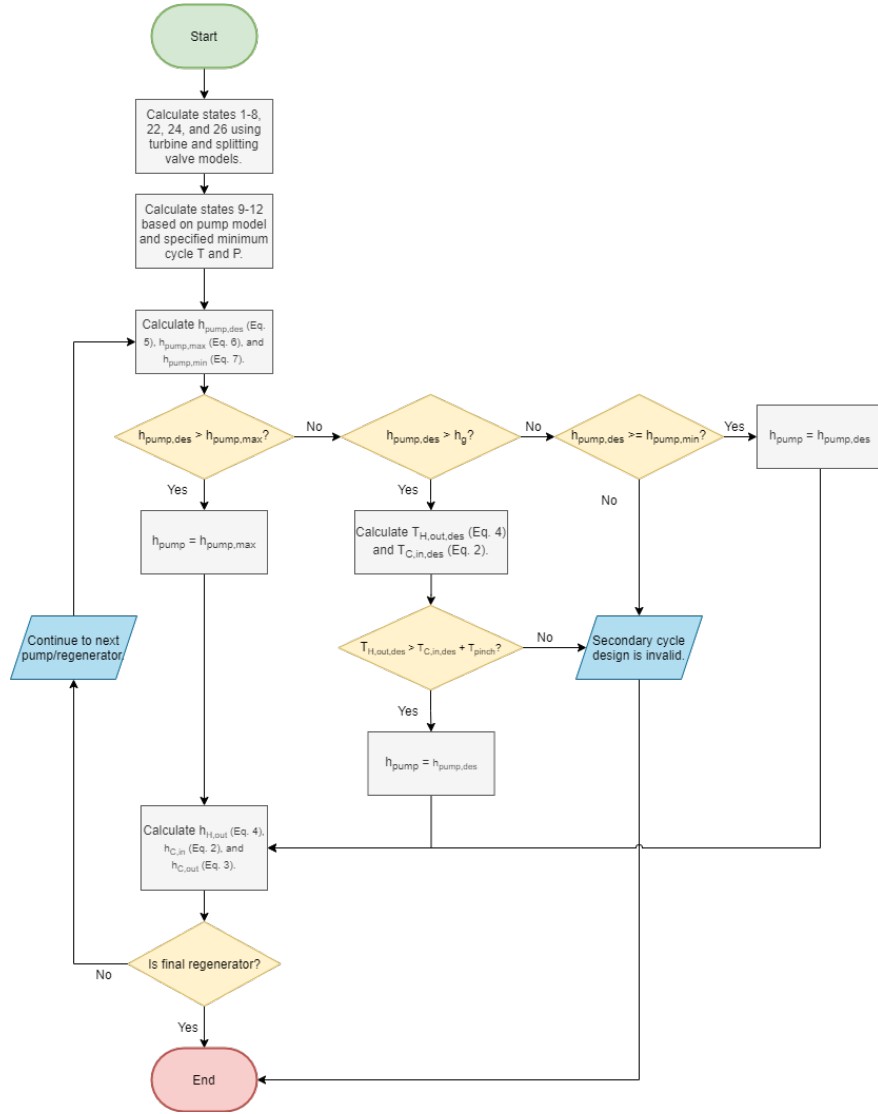$$\dot{m}_H (h_{H,in} - h_{H,out}) = \dot{m}_C (h_{C,out} - h_{C,in}). \tag{6}$$

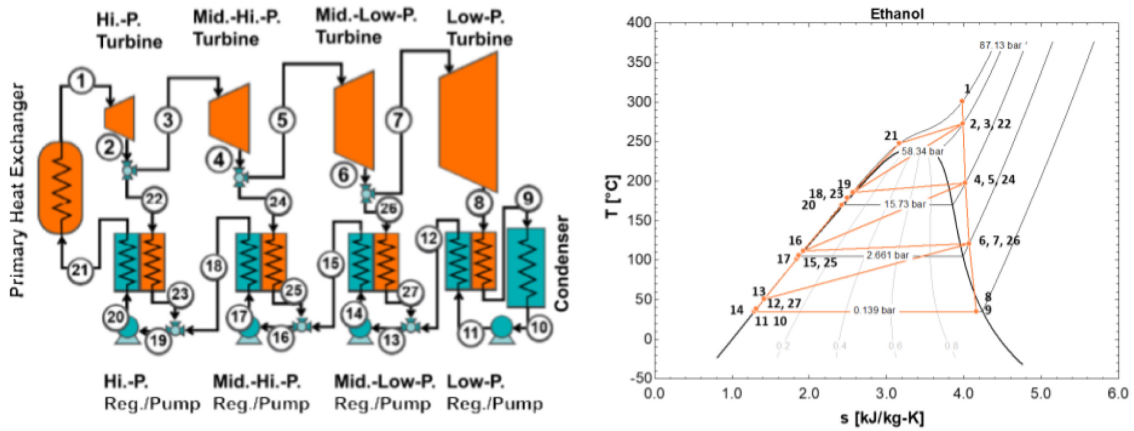Figure 2: Diagram of the solution method for the secondary cycle.

Figure 3: Cycle and T-s diagram for a transcritical cycle [15].

2.1.4. Splitting & Mixing Valves

Splitting valves divert a portion of the flow exiting a turbine to the regenerator and the remaining fluid to the next turbine. The mass fractions, which are among the specified design parameters, are defined to be the portion of the mass flow that is directed to the regenerator, so

$$f = \frac{\dot{m}_{regen}}{\dot{m}_{in}}.$$

There is no change in the fluid state between the inlet and outlet of the splitting valves.

Mixing valves combine the fluid exiting the hot side of a regenerator with that exiting the cold side of the upstream regenerator. By way of a simple energy balance,

$$h_{out} = \frac{\dot{m}_{in,1}h_{in,1} + \dot{m}_{in,2}h_{in,2}}{\dot{m}_{in,1} + \dot{m}_{in,2}}. \tag{7}$$

2.1.5. Pump/Regenerator Solver

When solving the states around a pump and regenerator (e.g. states 18-23 for the high pressure pump and regenerator), it is desirable to make the regenerator the smallest possible while still cooling the fluid on the hot side of the regenerator enough that the fluid at the pump inlet is a subcooled liquid, since any vapor entering the pump and severely reduce the service life of the pump. To this end, we attempt to specify the state at the pump inlet to be subcooled by 1°C. In other words,

$$
\begin{aligned}
T_{pump,des} &= T_f - 1°C \\
h_{pump,des} &= h(T = T_{pump,des}, P = P_{pump}).
\end{aligned}
\tag{8}
$$

However, it is not always possible to achieve this desired state for a given design point. The maximum enthalpy that the fluid can have at the pump inlet is

$$h_{pump,max} = \frac{h_{H,in}\dot{m}_H + h_u\dot{m}_u}{\dot{m}_H + \dot{m}_u}, \tag{9}$$

which corresponds to there being no regenerator and hot fluid entering the mixing valve directly from the turbine.

In the case that $h_g \leq h_{pump,des} < h_{pump,max}$, the pump and mixing valve models (Eqs. 5 and 7, respectively) are used to calculate the $h_{C,in}$ and $h_{H,out}$ values and their corresponding temperatures for $h_{pump,des}$. Then, if $T_{H,out,des} > T_{C,in,des} + \Delta T_{pinch}$, where ΔT_{pinch} is a small minimum temperature difference between the two sides of the regenerator, then the desired pump inlet state is valid. There are two main reasons to enforce this ΔT_{pinch} temperature difference: (1) it forces the size of the regenerator to be bounded, and (2) it serves as a safety net for approximations made around variable fluid properties. A value of 0.1°C was adequate for these purposes.

The minimum possible enthalpy at the pump inlet is more difficult to quantify. This is approximated by assuming the fluid on the hot side must condense and that the pinch point in the regenerator falls at neither the inlet nor the outlet, but where the hot side fluid enters the two-phase region. It then follows that the

$$h_{pump,min} = h_{s,out} + \eta_p \left[h_{C,pinch} - \left(1 - \frac{\dot{m}_H}{\dot{m}_C}\right) h_u - \frac{\dot{m}_H}{\dot{m}_C} \right], \tag{10}$$

where $h_{s,out}$ is the enthalpy at the outlet of the pump if the inlet state is the desired pump inlet state and if the pump were isentropic.

The pump inlet state has a valid solution if $h_{pump,des} \geq \min(h_{pump,min}, h_{pump,max})$, since it is not guaranteed that $h_{pump,max} > h_{pump,min}$ as they are defined. Then, if the desired state is valid,

$$h_{pump} = \min(h_{pump,des}, h_{pump,max}). \tag{11}$$

The remaining states in the pump/regenerator section can all be solved directly if h_{pump} is known. If the pump inlet state has no solutions in which the pump inlet state is not subcooled, the potential design point is rejected.

Once the true h_{pump} has been calculated, $h_{H,out}$ and $h_{C,in}$, and $h_{C,out}$ can be calculated with Eqs. 7, 5, and 6, respectively. The procedure is then repeated on the subsequent pump/regenerator section of the cycle.

This method is a departure from the pinch point method initially proposed in [15]. Analysis of the initial results from optimization when using the pinch point method indicated that the cycle tended towards designs with two-phase fluids at the pump inlets, despite penalization of these solutions. Extremely few design points sampled had no vapor at these pump inlet states. The number of points satisfying this constraint increased by several orders of magnitude by imposing this constraint with the solution method detailed above rather than through a penalization scheme.

2.2. Primary Heat Exchanger

The primary heat exchanger couples the secondary cycle to the SMR cycle. It is modeled by a system of ordinary differential equations in terms of enthalpy describing a one-dimensional counterflow heat exchanger,

$$
\begin{aligned}
\frac{di_P}{dx} &= -\frac{T_P(x) - T_S(x)}{\dot{m}_P R'_{tot}(x)} \\
\frac{di_S}{dx} &= -\frac{T_P(x) - T_S(x)}{\dot{m}_S R'_{tot}(x)},
\end{aligned}
\tag{12}
$$

where $T_P(x)$ and $T_S(x)$ are the mean temperatures of the primary- and secondary-side fluids at axial location x, respectively, and $R'_{tot}(x)$ is the total thermal resistance per unit length at x. See [15] for more details on the iterative solution for the convection coefficients necessary to solve for the total thermal resistance. The secondary-side outlet state is defined by the maximum temperature and pressure of the system and the primary side inlet state is fixed, so initial conditions can be defined at the primary side inlet/secondary side outlet according to those states. This system of ODEs is integrated numerically to determine the enthalpy of the primary and secondary fluids along the length of the heat exchanger. Pressure drop across the heat exchanger is neglected.

3. Optimization Methodology

The results of the thermodynamic model of the integrated cycles are used to calculate the LCOE of the given design point, which is to be optimized. This optimization problem is subject to a number of constraints, including bounds on the design variables, turbine expansion limits, and pump vapor qualities. More precisely, we seek to solve the following optimization problem:

$$
\begin{aligned}
\text{Minimize} \quad & \text{LCOE}(P_{max}, R_1, R_2, R_3, f_1, f_2, f_3) \\
\text{s.t.} \quad & 8.22 \text{ MPa} \leq P_{max} \leq 9.2 \text{MPa} \\
& 0 \leq R_1, R_2, R_3 \leq 1 \\
& 0 \leq f_1, f_2, f_3 \leq 1 \\
& Q_{turb} \geq 0.87 \\
& Q_{pump} = 0.
\end{aligned}
\tag{13}
$$

In the constraints of Eq. 13, the first three constraints enforce bounds on the optimized design parameters, the fourth constraint limits the turbine outlet vapor quality to 0.87, and the final constraint requires the vapor quality at the pump inlet to be zero (or be a subcooled liquid). These final two constraints cannot be easily formulated in terms of the optimized design parameters, and the calculations required to test if these constraints are satisfied are the same as those used to complete the solution of the secondary cycle.

Since these constraints cannot be formulated explicitly, they are treated as hidden constraints. This complicated the solution of the optimization problem substantially because potential design points cannot be generated solely in the region of the design space which satisfies all constraints. Instead, points satisfying the first three inequality constraints can be generated, but then the integrated cycle solution must be attempted on these points in order to determine if the remaining constraints are also met. This can lead to needing to sample far more points than yield useful solutions, which can be computationally taxing. Constraints which

cannot be verified for a given input point before attempting to evaluate the objective function are known as hidden constraints.

Fortunately, these hidden constraints can be checked relatively quickly in this case because they depend only on values in the secondary cycle solution. As seen in Figure 1, the secondary cycle solution is only weakly coupled to the primary cycle in the integrated cycle solution algorithm. They are linked by their respective mass flow rates since the primary cycle states are dependent on the amount of heat transferred to the secondary cycle, due to the primary cycle being driven by natural convection. However, all of the thermodynamic states of the secondary cycle can be solved without knowing the mass flow rate of the cycle since the ratio of mass flow rates on either side of the regenerators can be determined by the splitter valve mass flow ratios (f_1, f_2, f_3) alone. As a result, the quality of each state in question can be determined before the majority of the computational work for the full integrated cycle solution is performed.

This study seeks to perform a global optimization of the integrated power cycles over the full ranges of the design variables. To this end, three global optimization techniques were applied: uniform random search, differential evolution, and dual annealing. The uniform random search is used as a baseline to gauge the performance of the other more sophisticated algorithms, while also generating results for a large number of points distributed uniformly across the design space. These data can be used to estimate correlations between input variables and output metrics.

Differential evolution is an evolutionary algorithm similar to standard genetic algorithms, but is adapted to work more easily with real-valued variables instead of discrete variables. This algorithm is due to Storn and Price [21]. Differential evolution is a stochastic, direct-search (no gradients) global optimization method that uses "generations" of candidate solutions to search the design space. Parameters like the population size, mutation rate, and recombination constant allow the user to tune the algorithm to a desired amount of design space exploration. Dual annealing couples a generalized simulated annealing algorithm with a local search methodology for the accepted location. The "initial temperature" for the simulated annealing portion can be adjusted to facilitate a wide search of the design space [22].

The differential evolution and dual annealing algorithms were chosen due to being bounded, global optimization methods whose stochasticity can be tuned with various hyperparameters to ensure adequate exploration of the design space. In addition to being mathematically appropriate, both of these algorithms are easily accessible to Python users. Both algorithms are implemented in the optimization module of the extremely popular SciPy package for Python [23].

The uniform random search is used to both provide a benchmark optimization result for the other two algorithms and generate data that can be used to statistically characterize the model output space. A random search is an extremely brute force approach to an optimization problem, and as such, the differential evolution and dual annealing algorithms are expected to perform much better than the random search.

In order to function in the framework of a hidden constraint optimization problem, invalid design points were assigned a very large LCOE and an efficiency of zero. This technique introduces discontinuities in the output space which would be problematic for gradient-based methods but pose little difficulty for the direct-search methods applied here.

4. Results and Discussion

An initial optimization for LCOE was performed by uniform random search. Approximately 1.3 million design points were sampled, and only 2.56% of these sampled points resulted in valid designs. The best point sampled had an LCOE of \$70.95/MWh, a 17.5% decrease from the baseline \$86/MWh, and a first-law efficiency of 29.24%.

Among these data, the first mass flow ratio, f_1, correlated most strongly with LCOE, and the first second pressure ratio, R_2, correlated most strongly with first-law efficiency. All correlation coefficients between design variables and output values can be seen in Fig. 4a. The correlation coefficient measures the level of linear correlation between two variables by comparing the covariance between the two variables to the variances of the individual variables. It ranges between -1 and 1, with 1 being perfectly correlated, -1 being perfectly inversely correlated, and 0 being no correlation. While this measure is unable to capture nonlinear correlations, the data does not seem to exhibit any such nonlinear correlative behavior.

Figure 4: Global and local (near DE point) correlation coefficients between the design parameters and LCOE and η_I.

4.1. Comparison of Designs from Different Algorithms

After the initial exploration of the design space with a random search, the differential evolution and dual annealing algorithms were applied to the optimization problem. The design points obtained from the random search, differential evolution, and dual annealing algorithms are summarized in Table 1. The optimizations with differential evolution and dual annealing each took approximately 6 hours, running with 8 parallel processes on a consumer-grade workstation. This is roughly an order of magnitude faster than the random search performed previously.

All of the optimal design points fall roughly in the same region of the design space, varying most significantly in the R_2 and R_3 parameters. However, these are parameters which are least correlated with LCOE both globally and locally near the design point from differential evolution, as seen in Figure 4, which shows the correlation coefficient between the seven design parameters and the two output metrics. The similarity of the design points is reassuring and suggests that these points may lie near the true global minimum. Since the Differential Evolution and Dual Annealing points had essentially the same LCOE, a closer look was taken at their respective regions of the design space.

	Random Search	Differential Evolution	Dual Annealing
P_{max} (MPa)	8.320	8.225	8.220
R_1	0.0616	0.1335	0.2052
R_2	0.4720	0.2955	0.1920
R_3	0.6441	0.3060	0.1685
f_1 (10^{-3})	3.023	0.9791	0.1787
f_2 (10^{-3})	2.397	1.462	0.1380
f_3 (10^{-3})	50.46	59.81	32.65
η_I	29.24%	29.31%	28.84%
LCOE ($/MWh)	70.95 (-17.5%)	69.55 (-19.1%)	69.64 (-19.0%)

Table 1: Output optimal design points from three global optimization algorithms.

10

4.2. Comparison of LCOE- and Efficiency-Optimal Designs

Optimizations for economic and thermodynamic metrics can often have very different results [13]. This is seen very clearly in this study. Performing a similar optimization with the differential evolution algorithm but seeking to maximize first law efficiency (η_I), the resulting optimal secondary cycle design parameters are very different from those obtained when minimizing LCOE. In fact, while η_I increased from 29.31% to 32.87%, the LCOE increased significantly from \$69.55/MWh to \$93.27/MWh, which is an 8.5% increase relative to the baseline.

	Optimized LCOE	Optimized η_I
P_{max} (MPa)	8.225	9.137
R_1	0.1335	0.5018
R_2	0.2955	0.3001
R_3	0.3060	0.2254
f_1	0.0009791	0.2774
f_2	0.001462	0.1734
f_3	0.05981	0.1431
η_I	29.31%	32.87%
LCOE (\$/MWh)	69.55 (-19.1%)	93.27 (+8.5%)
$\dot{Q}_{in}$ (MW)	211.9	142.9
$\dot{m}_P$ (kg/s)	643.1	565.7
$\dot{m}_S$ (kg/s)	151.1	179.8

Table 2: Comparison of design points obtained when optimizing for efficiency and LCOE.

The LCOE- and efficiency-optimized design points are compared in Table 2. When optimizing for efficiency, the optimization lead to marked increases in P_{max}, R_1, f_1, f_2, and f_3. The only parameters largely unaffected by the change in objective function were those that had correlated least with LCOE in the economic optimization: R_2 and R_3. Greater pressure ratios (R_i) and splitter valve mass flow ratios (f_i) for the high-efficiency cycle mean that this more efficient cycle design point operates at higher pressures and lower mass flow rates in the later stages of the cycle, whereas nearly all of the fluid reaches the final turbine stage in the low LCOE cycle design point.

In fact, by keeping nearly all of the fluid flow running through the turbines and very little being redirected to the regenerator/pump sections, the low LCOE design point is able to completely eliminate the need for the regenerators in the interest of cost savings. Figure 5 shows the comparative costs of the components, grouped by component type. While the greater mass flow rates in the turbines leads to slightly higher turbine costs, eliminating the regenerators more than makes up that increase in cost. Only the mid-hi-P and hi-P regenerators are used by the high efficiency design point. The temperature profiles of these regenerators are seen in Figure 6. Since the geometries of these regenerators are not defined, the temperatures are plotted against a cumulative fraction of the total heat transfer area required for each regenerator. In both of these regenerators, the hot-side fluid remains a superheated vapor, and the role of the chosen ΔT_{pinch} can be seen in Figure 6b, which nearly exactly satisfies that minimum pinch temperature. Increasing the value of ΔT_{pinch} (i.e. truncating the Hi-P regenerator) would likely mean this design point would no longer be valid, due to the fluid leaving the hot side of the regenerator being too hot and causing there to be vapor at that pump inlet.

These two design points also behave radically differently in the primary heat exchanger. The low-LCOE cycle takes a much larger heat input than the high-efficiency cycle, operating with 211.9 MW and 142.9 MW transferred in the primary heat exchanger to the secondary cycle, respectively. A comparison of the temperature profiles in the primary heat exchanger is found in Figure 7. This large difference in heat transfer is due to a combination of the secondary cycle fluid having a much lower temperature entering the primary heat exchanger and a higher ratio of primary to secondary mass flow rates, $\dot{m}_P/\dot{m}_S$, in the low-LCOE cycle, with ratios of 4.257 for the low-LCOE cycle and 3.146 for the high-efficiency cycle.
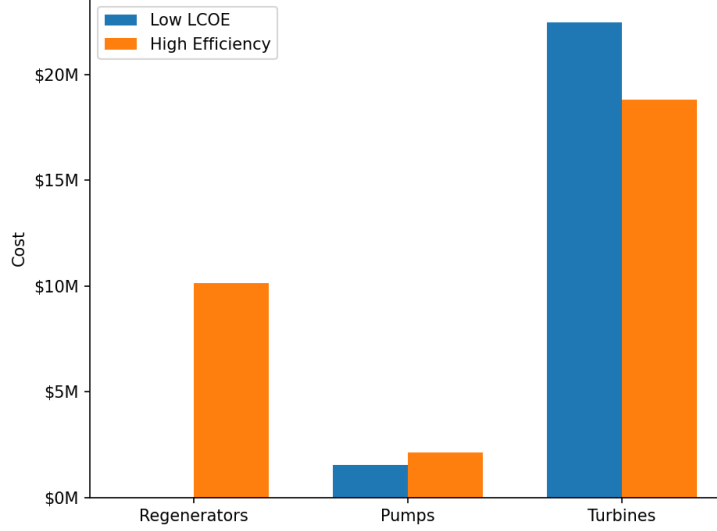
Figure 5: Component costs grouped by component type, comparing between the low LCOE and high efficiency design points.
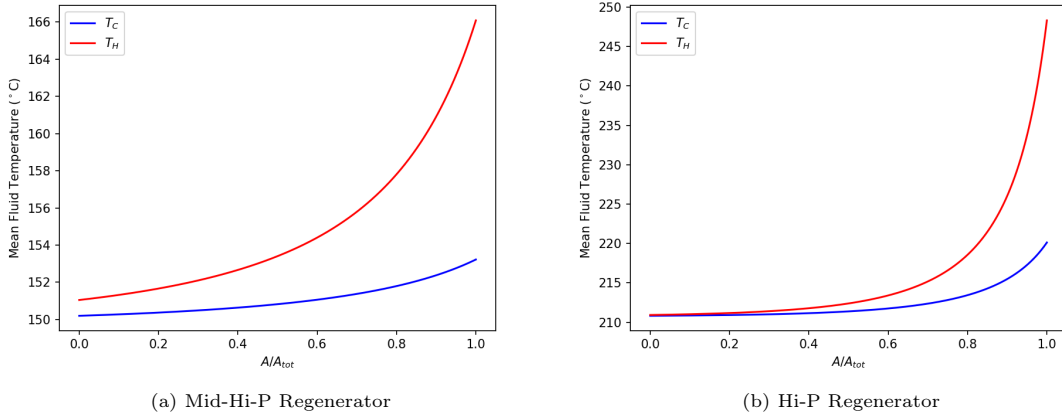

(a) Mid-Hi-P Regenerator

(b) Hi-P Regenerator

Figure 6: Temperature profiles of the mid-hi-P and hi-P regenerators in the high efficiency design point.

4.3. Characteristics of the Optimal Region

To further characterize the optimal regions, design points ($N = 116882$) were randomly sampled from a small region around both the differential evolution and dual annealing design points (± 0.05 for each design parameter). While the LCOE of each of these optimal points is nearly the same, the region around the differential evolution point had a greater percentage of valid points and a greater average efficiency with roughly the same average LCOE, so the results from the differential evolution region are presented here. A scatter plot of the percent change in LCOE relative to the baseline and first law efficiency of the valid design points with histograms of these output values found on their corresponding axes is found in Fig. 8.

While the differential evolution point (in red) does not have the lowest LCOE of the points sampled in this region, the optimization did quite well at capturing the minimum here. It is also of interest to see the trade-off between thermodynamic efficiency and cost efficiency here, where the points with the lowest LCOE have a mid-range first-law efficiency for this data set. Also, LCOE and first-law efficiency are roughly normally distributed, as seen by their respective histograms in Fig. 8, and they are essentially uncorrelated in this region ($R^2 = 0.008$).

Even in this small neighborhood of the optimum, only 62.1% of the sampled points were valid designs, so it is important to determine which constraints are being violated to have an idea of the feasibility of
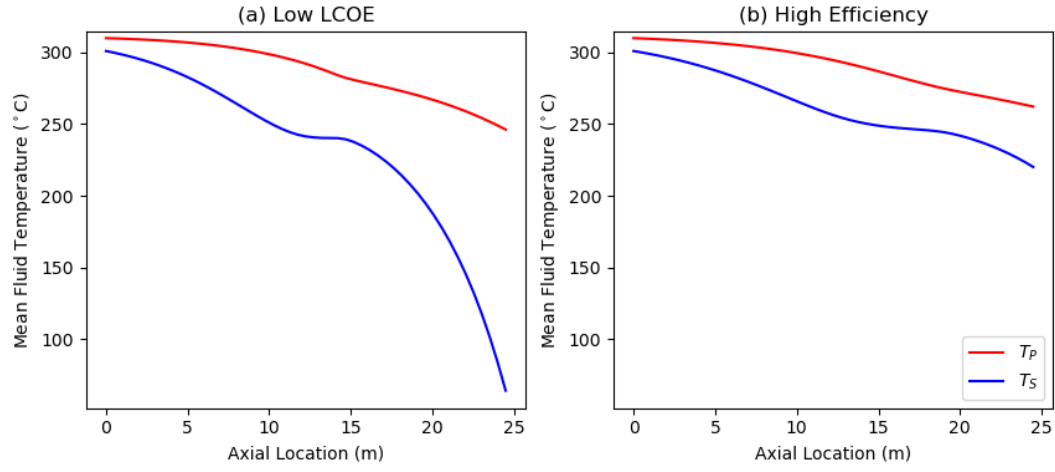
12

Figure 7: Temperature profiles of the primary and secondary cycle fluids in the primary heat exchanger for (a) the low-LCOE cycle and (b) the high-efficiency cycle.
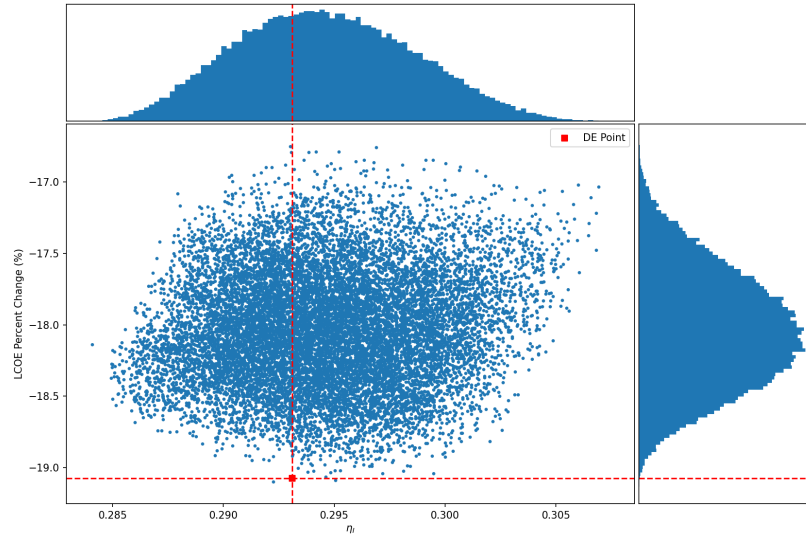

Figure 8: Valid design points from the region around the differential evolution optimum. Histograms on the x- and y-axes show the distribution of the outputs, and the red marker and lines show the location of the differential evolution point.

operating such a cycle. All of the points sampled in this region had $h_f < h_{pump,des} < h_g$ for the mid-low pressure pump, and the only model constraint causing potential design points to be invalid in this region is the mid-low pressure pump state vapor constraint. This simplifies the pump/regenerator solver sufficiently to arrive at an analytic expression for this validity boundary based on the pump/regenerator model outlined in Section 2.1.5. Here, this boundary is given as an inequality for values of mass fraction f_3 which will produce valid design points:

$$f_3 \leq \frac{(h_{isen,out} - h_{pump,des}) + \eta_p (h_u - h_{C,pinch})}{\eta_p (h_u - h_{g,H})}. \tag{14}$$

All of the enthalpies in this inequality are uniquely defined by pressures $P_C = P_{max} R_1 R_2$ and $P_H = P_{max} R_1 R_2 R_3$. The isentropic pump exit enthalpy $h_{isen,out}$ is calculated with the pump model (Eqs. 4 - 5) with $h_{pump,des}$ as the pump inlet enthalpy, h_u is the enthalpy of the fluid coming from the low-pressure pump/regenerator, $h_{g,H}$ is the saturated vapor enthalpy at the hot-side pressure, and $h_{C,pinch}$ is the enthalpy at $(P = P_C, T = T_{H,sat})$. It is important to note that this inequality only holds in a small region around the identified optimal design and is not valid globally, where other constraints may be violated.

The physical interpretation of this constraint is more clear when rewritten in the form

$$\dot{m}_H (h_{g,H} - h_{H,out,des}) \geq \dot{m}_C (h_{C,in,des} - h_{C,pinch}),$$

where $h_{H,out,des}$ and $h_{C,in,des}$ are the enthalpy states at the regenerator hot side outlet and cold side inlet, respectively, as calculated using $h_{pump,in} = h_{pump,des}$ and a fixed upstream fluid state. Now, we can see that this constraint is requiring that the heat difference on the hot side of the regenerator from the saturated vapor line to the desired outlet state must be greater than or equal to the heat difference from the desired regenerator cold side inlet to the pinch point. This means it is required that the pinch point occurs when the hot side fluid is somewhere in the two-phase region. In other words, the hot side fluid must be cooled down enough to begin condensing and exit with sufficiently low enthalpy for the relative mass flow rates, or the desired pump inlet state cannot be achieved. This makes intuitive sense, but having an explicit formulation (Eq. 14) of this requirement in terms of the design variables and enthalpies that are functions of the design variables allows this optimization problem to be transformed from a hidden optimization problem to an explicitly-constrained optimization problem. This distinction can have significant runtime benefits when the objective function becomes computationally expensive to evaluate.

Plotting this inequality as a function of these pressures in Fig. 9, it can be observed that the resulting surface does demark the validity boundary in this near-optimal region. Also, we can see that the surface is much more sensitive to P_H than P_C. Variations in P_{max} or any of the three pressure ratios could result in a sufficiently large change to P_H and cause vapor to appear at the pump inlet, so careful control of these variables is essential to operation in this region of the design space.

5. Conclusion

Transcritical Rankine cycles with organic working fluids like methanol are promising prospects for secondary power cycles in mid-temperature ranges. The optimization of an ORTC design here has shown that such a secondary power cycle could reduce the LCOE of a SMR by as much as 19%. Furthermore, characterization of the output space has yielded a locally-valid analytic expression for the design validity boundary in the neighborhood of the identified optimal design.

More work is needed to experimentally validate the designs presented here, specifically due to the volatility of fluid properties near their pseudo-critical points where the proposed cycle operates. Little such work has been performed for supercritical organic fluids. Experimentation could allow for refinement of the one-dimensional heat transfer models employed here.

Also, as with any non-convex global optimization problem, there is the potential that there is a better design - due to better LCOE, greater stability, or some other metric - that exists somewhere in the design space. However, further exploration becomes a computationally expensive task. In future work, we intend to explore the use of surrogate modeling to further reduce execution time in order to explore the design space more thoroughly and perform additional uncertainty and stability analyses around the proposed designs.

Finally, optimizing a slightly outdated model is less than ideal for immediate impact. However, the optimization performed here could be easily adapted to work with the updated NPM design figures and cost model. We hope to revisit this topic in the future.
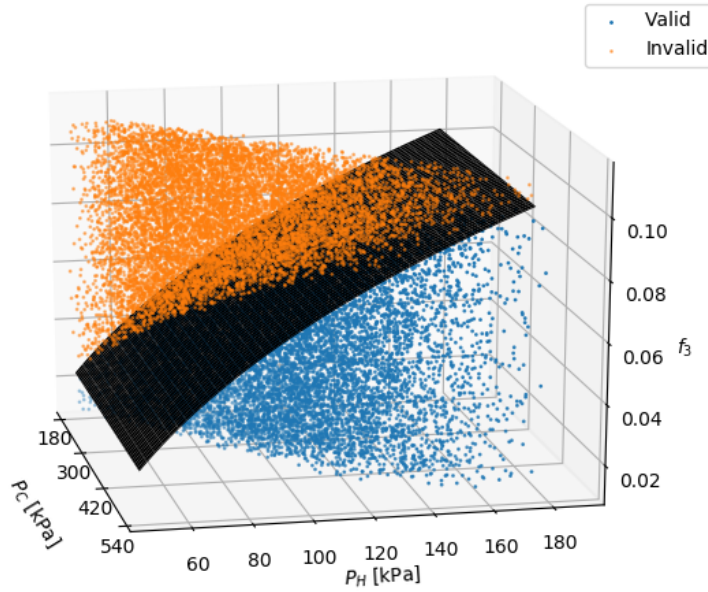
Figure 9: Validity surface in the region of the identified optimum design point.

Acknowledgements

References

[1] Fatih Birol. World Energy Outlook 2019. Technical report, IEA, Paris. URL https://www.iea.org/reports/world-energy-outlook-2019.

[2] Electric Power Monthly with Data for March 2021. Technical report, U.S. Energy Information Administration, May 2021. URL https://www.eia.gov/electricity/monthly/current$_m$onth/may2021.pdf.

[3] Lazard's Levelized Cost of Energy Analysis. Technical Report Version 14.0, Lazard, October 2020. URL https://www.lazard.com/media/451419/lazards-levelized-cost-of-energy-version-140.pdf.

[4] Jasmina Vujić, Ryan M. Bergmann, Radek Škoda, and Marija Miletić. Small modular reactors: Simpler, safer, cheaper? *Energy*, 45(1):288–295, September 2012. ISSN 0360-5442. doi: 10.1016/j.energy.2012.01.078. URL https://www.sciencedirect.com/science/article/pii/S036054421200093X.

[5] Upgrading America's Energy System. Technical report, NuScale Power, LLC, 2017.

[6] Featured Topic: Cost Competitive - NuScale's Affordable SMR Technology For All. *NUCLEUS*. URL https://www.nuscalepower.com/newsletter/nucleus-spring-2020/featured-topic-cost-competitive.

[7] Sylvain Quoilin, Martijn Van Den Broek, Sébastien Declaye, Pierre Dewallef, and Vincent Lemort. Techno-economic survey of Organic Rankine Cycle (ORC) systems. *Renewable and Sustainable Energy Reviews*, 22:168–186, June 2013. ISSN 1364-0321. doi: 10.1016/j.rser.2013.01.028. URL https://www.sciencedirect.com/science/article/pii/S1364032113000592.

[8] Yiping Dai, Jiangfeng Wang, and Lin Gao. Parametric optimization and comparative study of organic Rankine cycle (ORC) for low grade waste heat recovery. *Energy Conversion and Management*, 50(3):576–582, March 2009. ISSN 0196-8904. doi: 10.1016/j.enconman.2008.10.018. URL https://www.sciencedirect.com/science/article/pii/S0196890408004342.

[9] Evangelos Bellos and Christos Tzivanidis. Investigation of a hybrid ORC driven by waste heat and solar energy. *Energy Conversion and Management*, 156:427–439, January 2018. ISSN 0196-8904. doi: 10.1016/j.enconman.2017.11.058. URL https://www.sciencedirect.com/science/article/pii/S019689041731110X.

[10] Zhixin Sun, Jianpeng Lai, Shujia Wang, and Tielong Wang. Thermodynamic optimization and comparative study of different ORC configurations utilizing the exergies of LNG and low grade heat of different temperatures. *Energy*, 147:688–700, March 2018. ISSN 0360-5442. doi: 10.1016/j.energy.2018.01.085. URL https://www.sciencedirect.com/science/article/pii/S0360544218301038.

[11] Diego Vittorini, Roberto Cipollone, and Roberto Carapellucci. Enhanced performances of ORC-based units for low grade waste heat recovery via evaporator layout optimization. *Energy Conversion and Management*, 197:111874, October 2019. ISSN 0196-8904. doi: 10.1016/j.enconman.2019.111874. URL https://www.sciencedirect.com/science/article/pii/S0196890419308568.

[12] Hadi Rostamzadeh, Mohammad Ebadollahi, Hadi Ghaebi, and Afshar Shokri. Comparative study of two novel micro-CCHP systems based on organic Rankine cycle and Kalina cycle. *Energy Conversion and Management*, 183:210–229, March 2019. ISSN 0196-8904. doi: 10.1016/j.enconman.2019.01.003. URL https://www.sciencedirect.com/science/article/pii/S0196890419300263.

[13] Daniel Maraver, Javier Royo, Vincent Lemort, and Sylvain Quoilin. Systematic optimization of subcritical and transcritical organic Rankine cycles (ORCs) constrained by technical parameters in multiple applications. *Applied Energy*, 117:11–29, March 2014. ISSN 0306-2619. doi: 10.1016/j.apenergy.2013.11.076. URL https://www.sciencedirect.com/science/article/pii/S0306261913009859.

[14] Anandu Surendran and Satyanarayanan Seshadri. Design and performance analysis of a novel Transcritical Regenerative Series Two stage Organic Rankine Cycle for dual source waste heat recovery. *Energy*, 203:117800, July 2020. ISSN 0360-5442. doi: 10.1016/j.energy.2020.117800. URL https://www.sciencedirect.com/science/article/pii/S0360544220309075.

[15] Yili Zhang, Hailei Wang, Sean Kissick, and Derick Botha. Modeling and simulation of an integrated regenerative transcritical cycle with a small modular reactor. *Energy Conversion and Management*, 225:113278, December 2020. ISSN 0196-8904. doi: 10.1016/j.enconman.2020.113278. URL https://www.sciencedirect.com/science/article/pii/S0196890420308189.

[16] Sina Kazemi Bakhshmand, Rahim Khoshbakhti Saray, Keyvan Bahlouli, Hajar Eftekhari, and Afshin Ebrahimi. Exergoeconomic analysis and optimization of a triple-pressure combined cycle plant using evolutionary algorithm. *Energy*, 93:555–567, December 2015. ISSN 0360-5442. doi: 10.1016/j.energy.2015.09.073. URL https://www.sciencedirect.com/science/article/pii/S0360544215012839.

[17] Joshua Clarke, Laura McLay, and James T. McLeskey. Comparison of genetic algorithm to particle swarm for constrained simulation-based optimization of a geothermal power plant. *Advanced Engineering Informatics*, 28(1):81–90, January 2014. ISSN 1474-0346. doi: 10.1016/j.aei.2013.12.003. URL https://www.sciencedirect.com/science/article/pii/S1474034613000980.

[18] Z. Q. Wang, N. J. Zhou, J. Guo, and X. Y. Wang. Fluid selection and parametric optimization of organic Rankine cycle using low temperature waste heat. *Energy*, 40 (1):107–115, April 2012. ISSN 0360-5442. doi: 10.1016/j.energy.2012.02.022. URL https://www.sciencedirect.com/science/article/pii/S036054421200117X.

[19] Georg Gyarmathy. Foundations of a Theory of the Wet-steam Turbine. Technical report, Defense Technical Information Center, Fort Belvoir, VA, August 1966. URL `http://www.dtic.mil/docs/citations/AD0489324`.

[20] Aleksandr Leizerovich. *Wet-steam turbines for nuclear power plants*, volume 481. PennWell USA, 2005.

[21] Rainer Storn and Kenneth Price. Differential Evolution – A Simple and Efficient Heuristic for global Optimization over Continuous Spaces. *Journal of Global Optimization*, 11(4):341–359, December 1997. ISSN 1573-2916. doi: 10.1023/A:1008202821328. URL `https://doi.org/10.1023/A:1008202821328`.

[22] Y Xiang, D. Y Sun, W Fan, and X. G Gong. Generalized simulated annealing algorithm and its application to the Thomson model. *Physics Letters A*, 233(3):216–220, August 1997. ISSN 0375-9601. doi: 10.1016/S0375-9601(97)00474-X. URL `https://www.sciencedirect.com/science/article/pii/S037596019700474X`.

[23] Pauli Virtanen, Ralf Gommers, Travis E. Oliphant, Matt Haberland, Tyler Reddy, David Cournapeau, Evgeni Burovski, Pearu Peterson, Warren Weckesser, Jonathan Bright, Stéfan J. van der Walt, Matthew Brett, Joshua Wilson, K. Jarrod Millman, Nikolay Mayorov, Andrew R. J. Nelson, Eric Jones, Robert Kern, Eric Larson, C. J. Carey, İlhan Polat, Yu Feng, Eric W. Moore, Jake VanderPlas, Denis Laxalde, Josef Perktold, Robert Cimrman, Ian Henriksen, E. A. Quintero, Charles R. Harris, Anne M. Archibald, Antônio H. Ribeiro, Fabian Pedregosa, and Paul van Mulbregt. SciPy 1.0: fundamental algorithms for scientific computing in Python. *Nature Methods*, 17(3):261–272, March 2020. ISSN 1548-7105. doi: 10.1038/s41592-019-0686-2. URL `https://www.nature.com/articles/s41592-019-0686-2`. Number: 3 Publisher: Nature Publishing Group.